Available online at www.sciencedirect.com
SCIENCE DIRECT®
PERGAMON
International Journal of Heat and Mass Transfer 46 (2003) 4595–4611
International Journal of HEAT and MASS TRANSFER
www.elsevier.com/locate/ijhmt

Effective diffusivity and water-saturation distribution in single- and two-layer PEMFC diffusion medium

Jin Hyun Nam [1], Massoud Kaviany *

Department of Mechanical Engineering, University of Michigan, Ann Arbor, MI 48109-2125, USA

Received 17 January 2003; received in revised form 5 June 2003

Abstract

The formation–distribution of condensed water in diffusion medium of proton exchange membrane fuel cells, and its tendency to reduce the local effective mass diffusivity and to influence cell performance, are studied. First the local effective mass diffusivity of a fibrous diffusion medium is determined as a function of the local porosity and local water saturation, using the network model for species diffusion. Then using this along with the hydrodynamics of capillary, two-phase flow in hydrophobic porous media, the water formation rate (hydrogen–oxygen reaction), and condensation kinetics, the one-dimensional distribution of water saturation is determined and roles of fiber diameter, porosity, and capillary pressure on cell performance are explored. The results point to a two-layer medium (similar to the added conventional microlayer) which is then analyzed for optimum performance.

Keywords: Effective diffusivity; Proton exchange membrane fuel cell; Diffusion medium; Water saturation

1. Introduction

The repeating unit cell of PEMFC is composed of a membrane electrode assembly (a polymer electrolyte attached by two thin catalyst layers made of carbon particles with Pt impregnation), two diffusion media, and bipolar plates. The diffusion medium (and the bipolar plate guiding the gas distribution) needs to be optimized to enhance the cell performance. The cell potential $\Delta\varphi$ is [1]

$$\Delta\varphi = \Delta\varphi^o - \eta_o - \eta_a - \eta_c = \Delta\varphi^o - j_e r_t - k_a \ln\left(\frac{j_e}{j_{e,0}}\right) + k_c \ln\left(\frac{p_{H_2}^2 p_{O_2}}{p_{g,H_2O}^2}\right), \quad (1)$$

where $\Delta\varphi^o$ is the reversible electro-chemical potential, η_o is ohmic loss, η_a is activation loss, and η_c is concentration loss. The loss by diffusion and flow distribution (bipolar plate) is the concentration loss, which accounts for change in cell potential influenced by the partial pressures (concentrations) of reactant and product species at the catalyst layers.

The diffusion medium should have small diffusion resistance and high electrical conductivity, so carbon fiber paper is the primary material for diffusion medium (due to its good electric conductivity and corrosion resistance). In addition, its water transport characteristic should be optimized, since presence of liquid water has significant effect on gas transport. The proton conductivity of polymer electrolyte membrane (ohmic loss), the level of catalyst flooding (activation loss), and the effective diffusivity (concentration loss), all strongly depend on the water saturation in diffusion medium.

The effective electro-osmosis coefficient α_{eo} is an important measure that represents balance of water between the anode and cathode [2,3],

$$\dot{m}_{l,H_2O}|_{anode\to cathode} = M_{H_2O}\alpha_{eo}\frac{j_e}{F}, \quad (2)$$

which includes the effect of electro-osmosis (water molecules dragged by the flow of protons, from anode to

* Corresponding author.
E-mail address: kaviany@umich.edu (M. Kaviany).
[1] Also affiliated with School of Mechanical and Aerospace Engineering, Seoul National University, Korea.

0017-9310/$ - see front matter © 2003 Elsevier Ltd. All rights reserved.
doi:10.1016/S0017-9310(03)00305-3

Nomenclature

A_{lg}/V	liquid/gas specific interfacial area, m^2/m^3
A_{sf}/V	solid/fluid specific interfacial area, m^2/m^3
c	mole concentration, mole/m^3
$D_{m,i}$	mass diffusivity of species i, m^2/s
$\langle D_{m,i}\rangle$	effective diffusivity of species i, m^2/s
F	Faraday constant, C/mole
$f(\varepsilon)$	normalized porosity function
$g(s)$	normalized liquid saturation function
Δh_{lg}	heat of vaporization, J/kg
$J(S)$	Leverette J-function
j_e	current density, A/cm^2
$j_{e,0}$	exchange current density, A/cm^2
K	absolute permeability, m^2
K_{rl}	relative permeability of liquid water
$\langle k\rangle$	effective thermal conductivity, W/m K
k_a	Tafel slope, V
k_c	concentration loss constant, V
k_g	thermal conductivity of gas, W/m K
L	thickness of diffusion layer, m
M_i	molecular weight of species i, kg/mole
$\dot{M}_i$	mass flow rate of species i, kg/s
$\dot{m}_i$	mass flux of species i, kg/m^2 s
$\dot{n}_{gl,H_2O}$	volumetric condensation rate, kg/m^3 s
P	operation pressure, atm
p_i	partial pressure of species i, Pa
$\lvert dp_c/dS\rvert$	slope of capillary pressure, Pa
q	heat flux, W/m^2
R_g	universal gas constant, J/mole K
r_t	cell area specific electrical resistance, Ω cm
r_c	mean radius of curvature, m
s	liquid water saturation
s_{im}	immobile saturation
S	reduced liquid water saturation
S_0	surface reduced liquid saturation
T	operation temperature, K
$\langle T\rangle$	local equilibrium temperature, K
x_i	mole fraction of species i

Greek symbols

α_{eo}	effective electro-osmotic drag coefficient
α_m	mass accommodation coefficient
ε	porosity
$\Delta\varphi$	cell potential, V
Γ	uptake coefficient
γ	volumetric condensation coefficient, s^{-1}
η	potential loss, V
μ_l	viscosity of water, kg/m s
ρ_i	density of gas species i, kg/m^3
ρ_l	density of water, kg/m^3
σ	surface tension, N/m
θ_c	contact angle, degree

Subscripts

H_2O	water
O_2	oxygen
H_2	vapor
nw, w	non-wetting, wetting
l, g, s	liquid, gas, solid
lg	liquid/gas
c	capillary or coarse-fiber layer
f	fiber or fine-fiber layer

cathode) and the back diffusion (diffusion of water due to gradient of water content in membrane). At high current density, the electro-osmosis becomes dominant and the region of membrane near the anode is vulnerable to dry-out and large ohmic loss. To solve this problem the membrane is made thin to enhance the back diffusion. In practice, both fuel and air gases are humidified, to provide the desired water in the anode side of the membrane and to reduce the evaporation of water in the cathode side of membrane.

In cathode diffusion medium, the product water flows towards the channel through gas-phase diffusion or liquid-phase motion. The humidification of oxygen gas makes it difficult for diffusion, therefore, liquid water becomes ever present in the diffusion medium. At high current densities, the liquid flow rate increases due to increased condensation, and when the channel is at the local vapor saturation condition, liquid water flows out of diffusion medium and surface droplets are formed.

The presence of water saturation in the diffusion medium not only imposes more resistance to the oxygen diffusion toward the catalyst layer, it also influences the catalyst flooding (partial coverage of catalyst particles with liquid water). While the diffusion resistance is controlled by average saturation in the diffusion medium, the catalyst flooding depends on the water saturation near the catalyst layer. The carbon fiber paper used for diffusion medium is generally hydrophobized with PTFE (Teflon) to reduce water saturation, and this is expected to facilitate the water transport.

Here we begin by determining the dependence of the effective mass diffusivity of fibrous diffusion media on the local porosity and saturation (Section 2). Then we develop a capillary pressure model for the distribution and motion of water in the diffusion media (Section 3). Then we use these results to develop a two-layer diffusion medium for enhancement of cell performance (Section 4).

2. Local effective diffusivity

The effective diffusivity $\langle D_{m,i}\rangle$ of diffusion medium, is correlated with porosity ε and saturation s using normalized functions $f(\varepsilon)$ and $g(s)$, i.e.,

$$\langle D_{m,i}\rangle = D_{m,i} f(\varepsilon) g(s), \quad s = \frac{V_l}{V_p} = \frac{\varepsilon_l}{\varepsilon}, \tag{3}$$

where $D_{m,i}$ is the multi-component mass diffusivity in plain medium, s is the water saturation, and ε_l is volume fraction of liquid water.

The effective medium theory has been used to estimate the effective diffusivity [4–8], and for packed spherical particles it gives

$$\langle D_{m,i}\rangle = D_{m,i} f(\varepsilon) = D_{m,i}\varepsilon^{1.5}. \tag{4}$$

Mezedur et al. [9], for multi-length scale, particle-based porous media such as catalytic converter wash-coat, suggest

$$\langle D_{m,i}\rangle = D_{m,i} f(\varepsilon) = D_{m,i}[1-(1-\varepsilon)^{0.46}]. \tag{5}$$

The microstructure of their model is sintered spherical particle mixtures, with different pore size distributions and the applicable porosity range is rather small, around 0.3.

Tomadakis and Sotirchos [10] suggest a percolation-type correlation for random fibrous porous media, i.e.,

$$\langle D_{m,i}\rangle = D_{m,i} f(\varepsilon) = D_{m,i}\varepsilon\left(\frac{\varepsilon-\varepsilon_p}{1-\varepsilon_p}\right)^{\alpha}, \tag{6}$$

where ε_p is a percolation threshold, and α is an empirical constant. For porous media composed of two-dimensional, long and overlapping, random fiber layers, ε_p is found 0.11 and α is 0.521 and 0.785, for in-plane and cross-plane diffusion, respectively. Such percolation behavior in diffusion is a typical characteristic of fibrous porous media [11,12].

The liquid saturation restricts the gas diffusion by reducing the diffusion area and creating tortuous diffusion path, and this is commonly modeled by a normalized function $g(s)$ as

$$g(s) = (1-s)^m. \tag{7}$$

If the pore structure does not change with water saturation, $m = 1.5$ from prediction of the effective medium theory. Mezedur et al. [9] numerically determine $m = 0.71$ for their porous medium. Using the network model, we now determine $f(\varepsilon)$ and $g(s)$.

2.1. Network model

The diffusion media used in the PEMFCs are made of stacked, two-dimensional random carbon fiber mats, shown in Fig. 1(a). The fibers are assumed infinitely long in the x- and y-directions (in-plane) using periodic boundary conditions, and overlapping of the fibers is allowed (excluded from the solid volume).

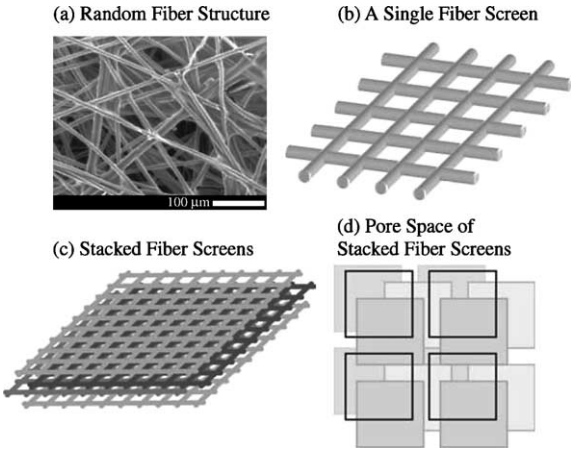

Fig. 1. Detailed microscale model for fibrous diffusion medium: (a) SEM of random fiber structure (a Toray carbon paper), (b) a single screen made of overlapping fibers with square pore spaces, (c) stack of fiber screens and (d) pore spaces of stacks, with an arbitrary screen position shifting.

Instead of constructing a pore network, we focus on the pore spaces surrounded by four intersecting fibers. The solid structure is modeled as stacks of continuously interwoven (overlapping) fiber screens (Fig. 1(b) and (c)) with regular, square pore spaces. The position of each layer is shifted by a randomly selected distances in plane, thus pores are connected to upper and lower pores, and the average coordination number for any one pore is 8 (Fig. 1(d)).

The porosity of diffusion media is around 0.5, and smaller than unused carbon fiber papers (0.7–0.8) due to compaction upon assembly. Then for the square geometry (Fig. 1(d)), we have

$$\varepsilon = \frac{l_p^2}{(l_p + l_f)^2}, \tag{8}$$

where l_p and l_f are the representative pore and fiber dimensions.

A total of 100 pore spaces (10×10) in a fiber screen are generated with periodic boundary condition. The cubic domain made of more than 50 layer of such fiber screens is discretized into small cubic volumes with l_f. Thus, a typical domain with porosity of 0.64 (l_f fiber diameter and $l_p = 4l_f$ pore size) is composed of $50\times50\times50$ cubic cells, prescribed as either pore or solid (occupied by fibers).

The diffusion mass flow of species i, between two adjacent (face-contacting) cells j and k, is

$$(\dot{M}_i)_{j-k} = \langle D_{\mathrm{m},i}\rangle A_{j-k}\frac{(\Delta\rho_i)_{j-k}}{l_{j-k}}, \tag{9}$$

where A_{j-k} and l_{j-k} are cross-sectional area and length for diffusion, and $(\Delta\rho_i)_{j-k}$ is the concentration difference of species i between the two cubic cells. For the given geometry, the face-conductance becomes equal to the effective mass diffusivity $\langle D_{\mathrm{m},i}\rangle$.

In addition to the above, there is an additional diffusion flux between two diagonal (edge-contacting) cells when they have a common, face-contacting solid cell (see cell I and IV in Fig. 2(a) which face-contact the solid cell II, in common). This is due to the circular cross-section of the fiber which allows for diffusion through small open space (fiber shoulder). Considering that the smallest open space is $0.143l_{\mathrm{f}}$ and the diffusion length is $2^{1/2}l_{\mathrm{f}}$, the edge-conductance (between two diagonal cells through a solid cell) can be roughly estimated to be 0.143 of the face-conductance.

The edge-conductance in the model does not significantly contribute in Fig. 2(a), because the main diffusion path between cell I and IV is the face-contacting cell III. However, for configuration shown in Fig. 2(b), if the edge-diffusion through the small throat between the two diagonally positioned fibers is not considered, the predicted effective diffusivity will be much smaller than it should be. More detailed about the edge-conductance is shown in Fig. 2(c).

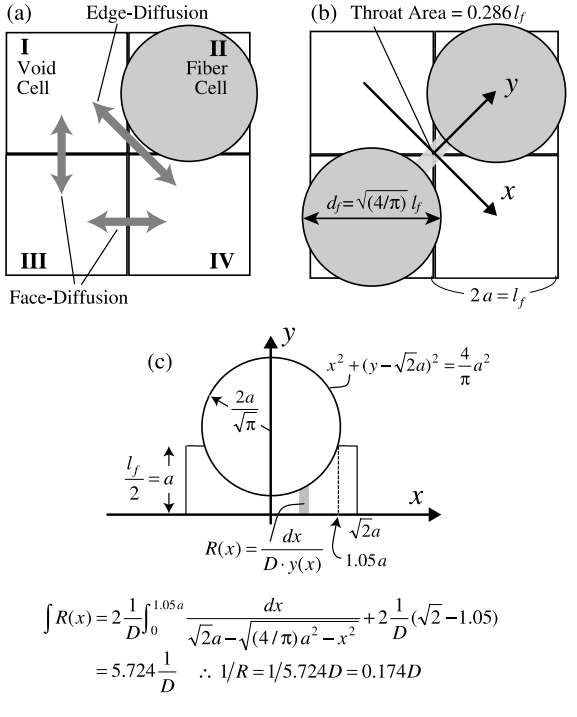

Fig. 2. Diffusion through the unit cells: cells I and IV communicate through cell III in (a) while they do not communicate in (b), if the edge-diffusion is not considered. In (c) detailed edge-conductance through a solid cell containing a fiber is presented. The ratio of the edge-diffusion conductance to the face-diffusion conductance is 0.174.

The liquid water droplets in hydrophilic fibrous media tend to extend their contact lines to the fibers, while in hydrophobic fibrous media, they tend to remain spherical, minimizing the contact lines. Possible topologies of water between fiber screens (different pseudo-droplet geometries) are shown in Fig. 3. The random spherical droplet scenario, Fig. 3(b), produces isotropic reduction in the effective diffusivity, while the others produce anisotropy.

There are two models for pore-filling water distribution, random and continuous (or correlated). If the liquid-phase does not contribute to the transport of product water, the water distribution can be discontinuous and a random distribution of water-filled pore spaces is found, depending on the saturation. Since the liquid-phase transport of product water is important, continuously connected water-filled pore spaces (to upper and lower screens), which we call correlated saturation distribution, is needed. The fully-correlated saturation will result in a pillar-type liquid water distribution, similar to that in Fig. 3(c). Then the cross-plane effective diffusivity will be almost a linear function of the liquid saturation (m in Eq. (13) approaches 1), as the tortuosity would not change much with this water distribution. Water droplets in hydrophobic diffusion medium are believed to be not fully random and not fully correlated, but intermediate.

2.2. Network computation

In absence of any net motion and reaction, we have the species conservation equation [13]

$$\nabla^2\rho_i = 0, \tag{10}$$

with boundary conditions for lower and upper boundaries of cubic domain,

$$\rho_i = \rho_{i,1} \text{ at lower boundary,}$$
$$\rho_i = \rho_{i,2} \text{ at upper boundary,} \tag{11}$$

and periodic boundary conditions for the other two directions. After the converged distribution of ρ_i (at all nodal locations) is obtained, the effective diffusivity is found from

$$\langle D_{\mathrm{m},i}\rangle = \frac{L}{\Delta\rho_i}\int \dot{m}_i\,\mathrm{d}A = \frac{L}{\rho_{i,1}-\rho_{i,2}}\int \dot{m}_i\,\mathrm{d}A. \tag{12}$$

Eq. (10) is solved by the Gauss–Siedel iteration with slight over-relaxation and a convergence criterion of 1×10^{-6}. The saturated (water-filled) pores are either randomly selected, or selected to obtain continuous liquid-phase flow path (contact to at least one saturated

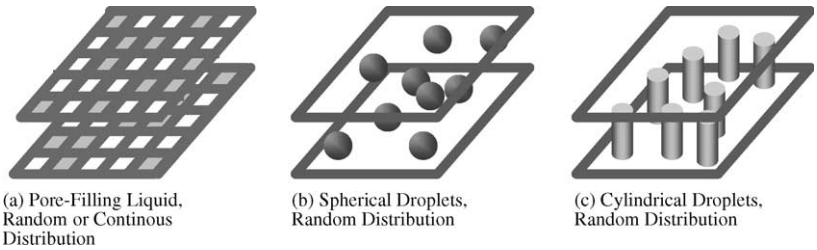

Fig. 3. Models for water droplet topologies in fibrous porous medium: (a) pore-filling, (b) spherical and (c) cylindrical.

pore at the neighboring upper and lower screens). Once $\rho_i(\boldsymbol{x})$ is converged and the fluxes for upper and lower boundaries are determined, the average of the two is used to determine the effective diffusivity. For each porosity and saturation, 10 set of different random networks are solved and then averaged.

2.3. Results and discussion

Variation of effective, cross-plane diffusivity with respect to porosity is shown in Fig. 4(a). The comparison with existing correlations shows a close agreement with that of Tomadakis and Sotirchos [10]. The estimated percolation threshold is between 0.2 and 0.3.

In Fig. 4(b), both the cross-plane and in-plane effective diffusivities are compared with the prediction of Tomadakis and Sotirchos [10]. The higher in-plane effective diffusivity is due to the alignment of fibers, where there is less blockage. When the porosity is as low as 0.44 ($l_p = 2l_f$ square pore), the predicted cross-plane diffusivity becomes larger than the in-plane. This is due to the intersection of fibers allowed in our

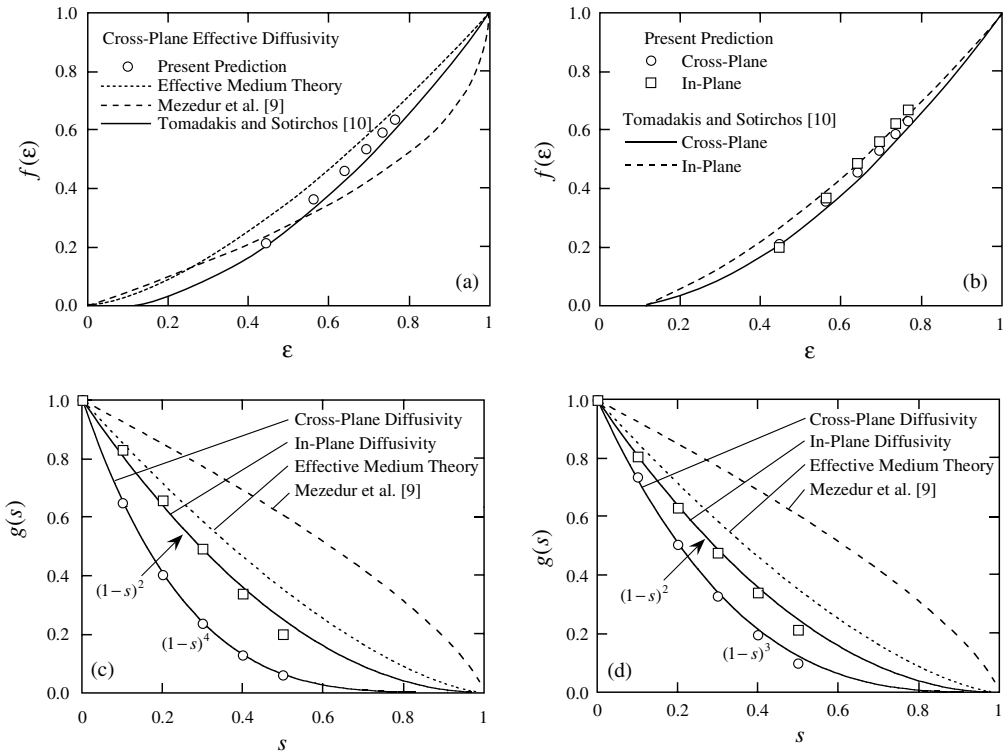

Fig. 4. Variation of the predicted effective diffusivity of fibrous diffusion media with respect to porosity and liquid water saturation: (a) comparison with effective cross-plane diffusivity correlations, (b) comparison with effective cross-plane and in-plane diffusivity of Tomadakis and Sotirchos [10], (c) the effect of liquid water saturation for randomly prescribed pore-filling water distribution and (d) for continuous pore-filling water distribution ($\varepsilon = 0.56$).

model (diffusion flux through two crossing fiber is ignored).

Two different water distribution is considered, and Fig. 4(c) and (d) show the variation of effective diffusivity for random and correlated water distribution, as a function of saturation. The $1-s$ dependence is always higher than 2. The cross-plane diffusivity is more significantly reduced in the presence of water, because the water droplets are assumed to have a thin rectangular shape, and more significantly increases the tortuosity for the cross-plane diffusion. The random distribution severely limits the effective, cross-plane diffusivity, while there is no significant difference between in-plane diffusivities with random and continuous water distribution. The continuous water distribution allows for the empty pores to also be continuous, which reduces the tortuosity for cross-plane diffusion.

A saturation of 0.5 reduces $\langle D_{\mathrm{m},i}\rangle$ by one orders of magnitude for cross-plane diffusion. Experimental results [14,15] also exhibit similar trend, significant reduction in effective diffusivity due to rather small liquid saturation. Recently Martys [16] numerically studied the effect of saturation in a porous medium with spherical incursions. The liquid water distribution was obtained by the lattice-gas calculation, and then used to define domain. The results show that for ideal wetting/non-wetting system, the $1-s$ dependence has a power of around 2. But for contact angle of 90° this is much larger than 2, which results in negligible gas diffusivity at saturation of 0.5.

The effective diffusivity as a function of saturation is shown in Fig. 5, for porosity of 0.56 and 0.64. Here we suggest (similar to [10]) as

$$\langle D_{\mathrm{m},i}\rangle = D_{\mathrm{m},i} f(\varepsilon) g(s) = D_{\mathrm{m},i}\varepsilon\left(\frac{\varepsilon-0.11}{1-0.11}\right)^{0.785}(1-s)^2. \tag{13}$$

3. Water saturation distribution

3.1. Modeling water transport in hydrophobic media

Water (non-wetting) in hydrophobic porous media preferentially resides in larger pores, where the curvature is decreased (with smaller contact area between the non-wetting phase and solid surface). The pressure difference between the wetting and non-wetting phase is given by the capillary pressure p_{c} as

$$p_{\mathrm{c}} = p_{\mathrm{nw}} - p_{\mathrm{w}} = p_{\mathrm{l,H_2O}} - p_{\mathrm{g}}. \tag{14}$$

This shows water pressure is higher and makes it possible to transport liquid water out of the hydrophobic diffusion medium without severe flooding, and also prevents wicking of water from the channels.

The water saturation in diffusion medium is not very large, which allows for a continuous gas phase with a uniform pressure. Then the gradient of the capillary pressure is

$$\nabla p_{\mathrm{c}} = \nabla p_{\mathrm{l,H_2O}} - \nabla p_{\mathrm{g}} = \nabla p_{\mathrm{l,H_2O}}. \tag{15}$$

We assume that the product water is in vapor phase and through non-equilibrium condensation of water vapor on the pre-existing liquid surface or condensation sites (hydrophobic coating defects), liquid water is introduced into the cathode diffusion medium. Fig. 6 shows two consecutive environmental scanning electron micrographs (ESEM), when a diffusion medium is exposed to a water saturated atmosphere (low temperature and small water vapor pressure). Our view of water transport is similar to the condensation and transport process shown in Fig. 6. When the liquid/gas interfacial area is large, the non-equilibrium condensation model approaches the equilibrium model. We focus on relatively high water saturation, where the channel is at vapor saturation condition, therefore, evaporation in the diffusion medium is negligible.

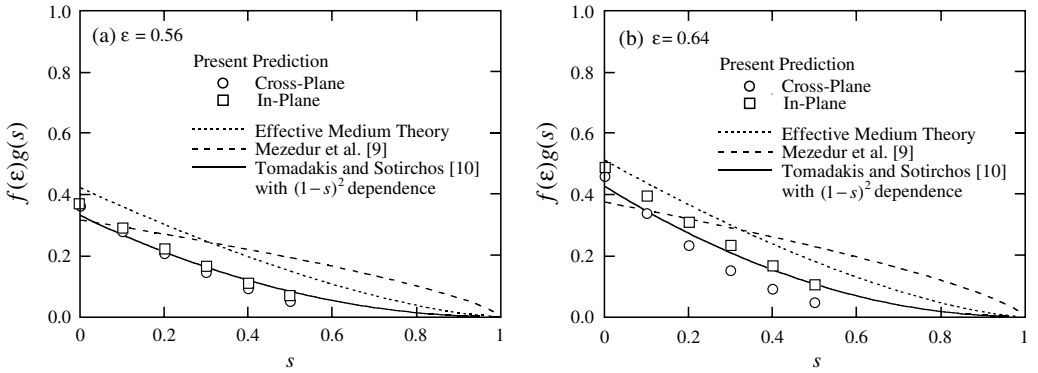

Fig. 5. Variation of the predicted effective diffusivity of fibrous porous diffusion medium with respect to local water saturation: (a) for $\varepsilon = 0.56$ and (b) for $\varepsilon = 0.64$.

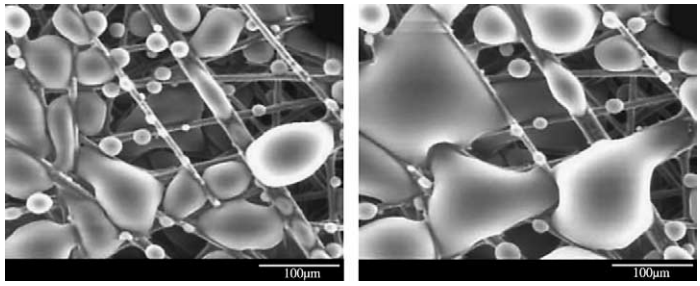

Fig. 6. Two consecutive environmental scanning electron micrographs (ESEM) of a diffusion medium exposed to water-vapor saturated atmosphere. In ESEM the sample is cooled such as only a small water vapor pressure is needed for condensation. The diffusion medium is a Toray carbon paper.

Two types of water transports, micro- and macro-transport, are believed to occur simultaneously. Near the catalyst layer a large number of condensation sites are activated to form micro-droplets, which agglomerates upon contacting with other liquid water bodies. As the spherical shapes of these small water droplets are less restricted by the solid structure, their capillary pressures are determined by the size of droplets. Thus, micro-transport of water occurs from small to large micro-droplets or from micro- to macro-droplets. Since droplet growth and agglomeration is a random process, the micro-transport does not contribute to the global (macroscopic) water transport. Instead, the role of micro-transport is transferring the condensed water from the condensation sites towards the flowing macro-droplets.

The micro-droplets continue to agglomerate to make pore-filling water droplets until a continuous liquid-phase (macro-droplets) is formed by reaching the threshold of the immobile saturation s_{im}. The macro-transport of water through this flow path, composed of connected many macro-droplets, occurs toward lower saturation region (toward the channel), as the pressure of liquid water is higher in the high saturation region no matter what the wetting phase may be (hydrophobic or hydrophilic). While flowing towards the channel, water preferentially selects larger pores, since it requires smaller capillary pressure and lower flow resistance.

Based on the above, the distribution of water is assumed to be the branching-type geometry shown in Fig. 7. The topology is composed of large main streams and smaller streams, connected to homogeneously distributed condensation sites. Water vapor condenses at the surface of the micro-droplets (rather uniformly distributed), which intermittently agglomerate to provide the macro-droplets with liquid water. The large main streams is extended from the catalyst layer to the channel, in order to transport the accumulated water through capillary motion. While large streams act as backbones for the macro-transport, smaller streams transport condensed water from the micro-droplets to the macro-droplets. Then the distribution of water in the capillary porous diffusion medium is controlled by condensation (micro-droplets) and by liquid-phase capillary flow (macro-droplets).

3.2. Capillary transport

Condensation and capillary motion of the condensate has been analyzed in [17]. The local water mass flux induced by capillary pressure is [18]

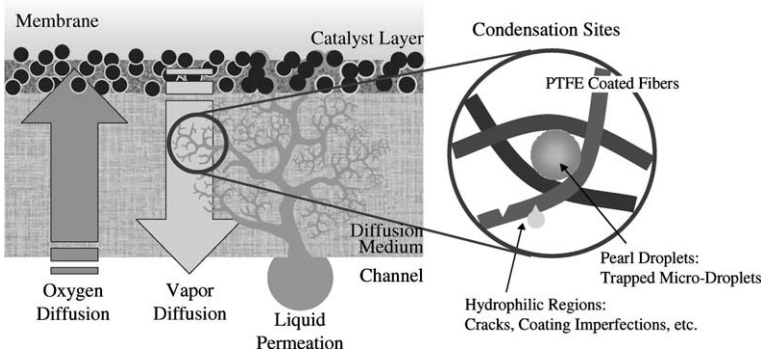

Fig. 7. Rendering of the water transport model, showing the branching micro- to macro-transport.

$$\dot{\boldsymbol{m}}_{\mathrm{l,H_2O}} = -\frac{\rho_{\mathrm{l}} K K_{\mathrm{rl}}}{\mu_{\mathrm{l}}} \nabla p_{\mathrm{c}} = -\frac{\rho_{\mathrm{l}} K K_{\mathrm{rl}}}{\mu_{\mathrm{l}}} \left(\frac{\mathrm{d}p_{\mathrm{c}}}{\mathrm{d}S} \right) \nabla S, \tag{16}$$

where S is reduced water saturation

$$S = \frac{s - s_{\mathrm{im}}}{1 - s_{\mathrm{im}}}. \tag{17}$$

The capillary water flow in (both hydrophobic and hydrophilic) porous media occurs always from the higher saturation region towards the lower saturation region. However, hydrophillic porous media wick in water from the surface due to the lower water pressure.

Along with the local water flux equation, there is a local volumetric condensation rate $\dot{n}_{\mathrm{gl,H_2O}}$

$$\dot{n}_{\mathrm{gl,H_2O}} = M_{\mathrm{H_2O}} \gamma \frac{p_{\mathrm{g,H_2O}} - p_{\mathrm{H_2O}}(T)}{R_{\mathrm{g}} T}, \tag{18}$$

where γ is the volumetric condensation coefficient that depends on kinetics of the condensation resistance, diffusion resistance, and liquid/gas specific interfacial area A_{lg}/V.

3.3. Transport parameters

Microscopically, the capillary pressure is a function of the curvature of the liquid/gas interface, i.e., the diameter in case of a spherical droplet. Due to the complex pore structure of the fibrous porous media, the curvature of liquid/gas interface is not easy to determine. As the curvature of liquid/gas interface is governed by how the wetting and non-wetting phases partition the available void space in porous medium, saturation can be used to estimate the curvature and the capillary pressure. The Leverett J-function is generally used for the capillary pressure versus saturation behavior, i.e.,

$$p_{\mathrm{c}} = p_{\mathrm{l,H_2O}} - p_{\mathrm{g}} = \frac{\sigma \cos\theta_{\mathrm{c}}}{(K/\varepsilon)^{1/2}} J(S)$$

$$= \frac{\sigma \cos\theta_{\mathrm{c}}}{(K/\varepsilon)^{1/2}} [1.417S - 2.120S^2 + 1.263S^3], \tag{19}$$

where term $(K/\varepsilon)^{1/2}$ is related to characteristic capillary radius r_{c} as

$$r_{\mathrm{c}} = 2(K/\varepsilon)^{1/2} \propto \frac{\varepsilon}{1-\varepsilon} d_{\mathrm{f}}. \tag{20}$$

In Eq. (16), we note that $(\mathrm{d}p_{\mathrm{c}}/\mathrm{d}S)$ is important and by differentiating Leverett J-function we obtain $(\mathrm{d}p_{\mathrm{c}}/\mathrm{d}S)$ as a function of reduced saturation. However, for simplicity, a constant slope $|\mathrm{d}p_{\mathrm{c}}/\mathrm{d}S|$ is used for the analysis instead of $(\mathrm{d}p_{\mathrm{c}}/\mathrm{d}S)$. We have estimated this linear slope for reduced saturation in the range from 0 to 0.5, and a good correlation is found between the linear slope by Leverett J-function and that by the measured pore size distribution (for a fibrous diffusion).

The empirical Kozeny–Carman relation is used to estimate the absolute permeability K [18]

$$K = \frac{\varepsilon^3 d_{\mathrm{f}}^2}{16 k_{\mathrm{K}} (1-\varepsilon)^2}, \tag{21}$$

where k_{K} is Kozeny constant and for fibrous media $(0.5 < \varepsilon < 0.7)$, this constant is taken as 6.

The flow in a partially saturated porous medium, is strongly dependent on the local saturation, similar to the effective diffusivity. For the relative permeability for liquid phase K_{rl}, we used [18]

$$K_{\mathrm{rl}} = S^3. \tag{22}$$

In general, a larger contact angle is preferred for a more efficient transport of the liquid water in the diffusion medium. The contact angle θ_{c} of a liquid droplet is defined as [18]

$$\cos\theta_{\mathrm{c}} = \frac{\sigma_{\mathrm{sg}} - \sigma_{\mathrm{sl}}}{\sigma}. \tag{23}$$

The intrinsic contact angle for the hydrophobic coating (PTFE) is about 108° when measured for water droplets on flat and smooth surface.

Hydrophobic surfaces with a significant roughness exhibit super-hydrophobicity ($\theta_{\mathrm{c,a}} > 170°$), with an apparent contact angle $\theta_{\mathrm{c,a}}$ larger than the intrinsic contact angle. A simple equation for the apparent contact angle, considering roughness, is [19]

$$\cos\theta_{\mathrm{c,a}} = \phi_{\mathrm{s}}(\cos\theta_{\mathrm{c}} + 1) - 1, \tag{24}$$

where ϕ_{s} is the ratio of the actual solid/liquid contact area under the droplet to nominal base area. For a 50% contact by the droplets ($\phi_{\mathrm{s}} = 0.5$) and for $\theta_{\mathrm{c}} = 90$–$120°$, $\theta_{\mathrm{c,a}} = 120$–$140°$.

We assume that the apparent contact angle of water in diffusion medium is about 120° ($|\cos\theta_{\mathrm{c,a}}| = 0.5$).

The statistical threshold saturation for the phase continuity in porous media is the immobile saturation s_{im}. The immobile saturation in diffusion medium is related to the invasion percolation [22], except that the water is introduced by condensation within the medium. Nucleation/percolation concept is reported by Du and Yortsos [23] in context of a critical gas saturation for formation of the continuous non-wetting gas phase (bubble) in a porous medium, saturated with the wetting liquid. The critical gas saturation depends on the number density of the activated nucleation sites, which implies that the immobile saturation of diffusion medium can be higher than that predicted by the invasion percolation.

Morrow [24] has conducted an extensive experiment on the irreducible saturations in spherical particle packings, with different particle size, size distribution, contact angle, etc. The measured irreducible saturations s_{ir} were similar regardless of the variation of physical

properties, but significantly increased when a spatial heterogeneity was introduced. Considering this, we assume that the immobile saturation of the diffusion medium is $s_{im} = 0.1$, because the spatial heterogeneity is minimal in the random fibrous diffusion medium.

Heterogeneous condensation of water vapor occurs in diffusion medium and requires a pre-existing liquid layer or the existence of a hydrophilic region, on the fiber surface. From the kinetic theory, the condensation rate (per unit interfacial area) is [20]

$$\dot{m}_{gl,H_2O} = \frac{1}{4}\bar{u}_m \alpha_m M_{H_2O} \frac{p_{g,H_2O} - p_{H_2O}(T)}{R_g T}, \tag{25}$$

where $\bar{u}_m$ is mean molecular speed $(8R_gT/\pi M)^{1/2}$, and α_m is the mass accommodation coefficient which is measured to be between 0.01 and 0.07 (0.04 used here).

The condensation rate is also limited by mass diffusion and heat transfer. Due to condensation of vapor at the liquid/gas interface, there are more non-condensable species present adjacent to the interface. Using an uptake coefficient Γ, we have

$$\dot{m}_{gl,H_2O} = \frac{1}{4}\bar{u}_m \Gamma M_{H_2O} \frac{p_{g,H_2O} - p_{H_2O}(T)}{R_g T}, \tag{26}$$

$$\frac{1}{\Gamma} = \frac{1}{\alpha_m} + \frac{\bar{u}_m l_D}{4D_{m,H2O}} = \frac{1}{\alpha_m} + \frac{3}{4}\frac{1}{Kn}, \tag{27}$$

where l_D is the characteristic length for diffusion, and Kn is the Knudsen number defined as λ/l_D (mean free path λ of water vapor at 1 atm and 70 °C is 0.05 μm). Assuming l_D is 10 μm, we obtain $Kn = 0.005$ and $\Gamma = 0.006$.

The volumetric condensation rate is

$$\begin{aligned}\dot{n}_{gl,H_2O} &= \dot{m}_{gl,H_2O}\frac{A_{lg}}{V} \\ &= \frac{1}{4}\frac{A_{lg}}{V}\bar{u}_m \Gamma M_{H_2O}\frac{p_{g,H_2O} - p_{H_2O}(T)}{R_g T} \\ &= \gamma M_{H_2O}\frac{p_{g,H_2O} - p_{H_2O}(T)}{R_g T}.\end{aligned} \tag{28}$$

and for 70 °C and 1 atm, the volumetric condensation coefficient γ is estimated to be $0.9A_{lg}/V$.

The liquid/gas specific interfacial area A_{lg}/V depends on the water saturation and a maximum 20% of the solid/fluid specific interfacial area A_{sf}/V was obtained [21] for hydrophilic spheres packings at small water (wetting) saturation. Due to hydrophobicity and fibrous medium, we assumed that the liquid/gas specific interfacial area is uniform (independent of local water saturation), since the micro-droplets are assumed to be uniformly distributed in the diffusion medium.

The liquid water condensed in diffusion medium moves towards the channel and forms droplets on that surface which in turn would evaporate or be mechanically removed. The surface saturation s_0 denotes the liquid water saturation adjacent to the diffusion medium/channel interface. The fraction of surface area covered by water droplets is not the same as the surface saturation, so we use the surface coverage for that. The lower bound for this surface saturation is the immobile saturation (which is the smallest saturation for a continuous liquid distribution).

Consider that the liquid water accumulated within the diffusion medium flows through a hydrophobic, circular pore (diameter d_p) to enter the channel and form a droplet. For this to happen, the liquid water pressure should exceed the breakthrough pressure $(4\sigma\cos\theta/d_p)$ of that capillary pore by a sufficient saturation accumulation. After the breakthrough, the liquid water pressure should remain higher than $2\sigma\cos\theta/d_p$ to secure the pore for liquid flow. Using this, the capillary breakthrough experiments (with a very thin diffusion medium) or invasion simulation with a realistic pore network model can be used to infer minimum surface saturation.

The surface saturation is believed to depend on the current density and the channel condition, and the two-phase flow characteristics of the diffusion medium. In general, s_0 increases with the rate of liquid-phase flow out of the diffusion medium, with the current density, and with the channel humidity.

3.4. Summary of one-dimensional governing equations

Based on the above mathematical formulations and transport parameters, the water distribution in the diffusion medium is obtained from the conservation equations and the constitutive relations. This is rendered in Fig. 8 and a list of the major parameters is also given.

Assuming a local thermal equilibrium among the phases, the one-dimensional, steady-state energy conservation equation with dominance of conduction becomes [25]

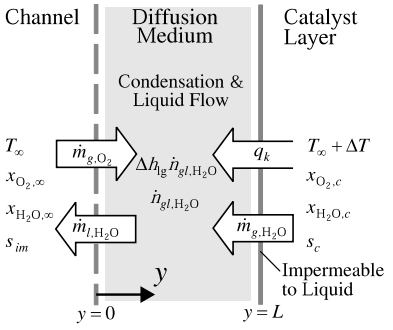

Fig. 8. Rendering of the one-dimensional transport problem in the diffusion medium.

$$\frac{\mathrm{d}}{\mathrm{d}y}\left[-\langle k\rangle\frac{\mathrm{d}\langle T\rangle}{\mathrm{d}y}\right]=\Delta h_{\mathrm{lg}}\dot{n}_{\mathrm{gl,H_2O}}, \tag{29}$$

and at the diffusion medium/catalyst layer interface ($y=L$), we have

$$-q_k=a_1(\Delta\varphi^o-\Delta\varphi)j_{\mathrm{e}}-\alpha_{\mathrm{eo}}M_{\mathrm{H_2O}}\frac{j_{\mathrm{e}}}{F}\Delta h_{\mathrm{lg}}, \tag{30}$$

and at the diffusion medium/channel interface ($y=0$), we have (assuming dominance of the internal resistance)

$$T=T_\infty, \tag{31}$$

where T_∞ is the prescribed temperature. The same assumption is also applied to concentration, i.e., the surface concentrations are equal to those of the local channel conditions.

The species conservation equation for oxygen is

$$\frac{\mathrm{d}}{\mathrm{d}y}\left[-cM_{\mathrm{O_2}}\langle D_{\mathrm{m,O_2}}\rangle\frac{\mathrm{d}x_{\mathrm{O_2}}}{\mathrm{d}y}+x_{\mathrm{O_2}}M_{\mathrm{O_2}}\sum_i\frac{\dot{m}_i}{M_i}\right]=0, \tag{32}$$

where c is total mole concentration ($P/R_{\mathrm{g}}T$), $\dot{m}_i$, is mass flux, and M_i is molecular weight of species i. At the diffusion medium/catalyst layer interface, we have

$$-\dot{m}_{\mathrm{O_2}}=-M_{\mathrm{O_2}}\frac{j_{\mathrm{e}}}{4F}, \tag{33}$$

and at the diffusion medium/channel interface, we have

$$c_{\mathrm{O_2}}=c_{\mathrm{O_2},\infty}, \tag{34}$$

where $c_{\mathrm{O_2}}$ is the mole concentration of oxygen, determined as $c_{\mathrm{O_2}}=cx_{\mathrm{O_2}}$.

Similarly, the species conservation equation for water vapor is

$$\frac{\mathrm{d}}{\mathrm{d}y}\left[-cM_{\mathrm{H_2O}}\langle D_{\mathrm{m,H_2O}}\rangle\frac{\mathrm{d}x_{\mathrm{H_2O}}}{\mathrm{d}y}+x_{\mathrm{H_2O}}M_{\mathrm{H_2O}}\sum_i\frac{\dot{m}_i}{M_i}\right]=-\dot{n}_{\mathrm{gl,H_2O}}, \tag{35}$$

and at the diffusion medium/catalyst layer interface, we have

$$-\dot{m}_{\mathrm{g,H_2O}}=M_{\mathrm{H_2O}}\frac{j_{\mathrm{e}}}{2F}(1+2\alpha_{\mathrm{eo}}), \tag{36}$$

and at the diffusion medium/channel interface, we have

$$c_{\mathrm{H_2O}}=c_{\mathrm{H_2O},\infty}. \tag{37}$$

The volumetric condensation rate $\dot{n}_{\mathrm{l,H_2O}}$ is given by Eq. (18) and the saturation water vapor pressure is approximated by

$$p_{\mathrm{H_2O}}(T)=\exp\left(-\frac{5800}{T}+1.391-0.4864T+0.4176\times10^{-4}T^2-0.1445\times10^{-7}T^3+6.546\ln(T)\right). \tag{38}$$

The liquid mass conservation equation with a volumetric condensation is

$$\frac{\mathrm{d}}{\mathrm{d}y}\left[-\rho_{\mathrm{l}}\frac{KK_{\mathrm{rl}}}{\mu_{\mathrm{l}}}\left(\frac{\mathrm{d}p_{\mathrm{c}}}{\mathrm{d}S}\right)\frac{\mathrm{d}S}{\mathrm{d}y}\right]=\dot{n}_{\mathrm{gl,H_2O}}, \tag{39}$$

and at the diffusion medium/catalyst layer interface, we have (s_{c} is designation of saturation at this interface)

$$\dot{m}_{\mathrm{l,H_2O}}=0, \tag{40}$$

and at the diffusion medium/channel interface, we have

$$S=S_0=\frac{s_0-s_{\mathrm{im}}}{1-s_{\mathrm{im}}}, \tag{41}$$

where s_0 is the prescribed surface saturation.

3.5. Results and discussion

The results presented in Figs. 9 and 10 are for the base parameters given in Table 1. Fig. 9(a) shows the saturation distribution across the diffusion medium, where the most noticeable variations are near the channel interface. This is due to the highly non-linear dependence of the relative permeability on saturation and also due to the distributed condensation. The condensation flux $\dot{m}_{\mathrm{gl,H_2O}}$ is higher near the catalyst layer, but the resulting water flux $\dot{m}_{\mathrm{l,H_2O}}$ is larger near the channel, as shown in Fig. 9(c). The mole fraction distribution of the water vapor shown in Fig. 9(b) indicates that thermodynamic equilibrium model can be used when the condensation rate is sufficiently large. The small vapor flux towards catalyst layer near the channel (shown as negative vapor flux in Fig. 9) indicates that water vapor diffuses into the diffusion medium along with the oxygen diffusion flux which becomes dominant where the vapor flux is negligible due to condensation.

Fig. 10(a) shows the variation of cell voltage and saturation adjacent to catalyst layer s_{c} as a function of the current density. The limiting current density $j_{\mathrm{e,lim}}$ shown in Fig. 10(a) corresponds to the oxygen diffusion limit, shown in Fig. 10(b). The water saturation at the diffusion medium/catalyst layer interface (s_{c}) also varies non-linearly, due to the relative permeability function. The temperature difference and the concentrations change almost linearly with increase in the current density, as shown in Fig. 10(b). The temperature difference across the diffusion medium ΔT is smaller than 1 K for ordinary operation condition ($j_{\mathrm{e}}<1$ A/cm^2) similar to Shimpalee and Dutta [26], which validates the use of isothermal assumption in the thickness direction.

The effect of liquid/gas specific interfacial area A_{lg}/V on the condensation rate is considered in Fig. 11(a) and (b). For $A_{\mathrm{lg}}/V>1000$ m^2/m^3, the entire water vapor condenses within the 500/m thickness of the diffusion

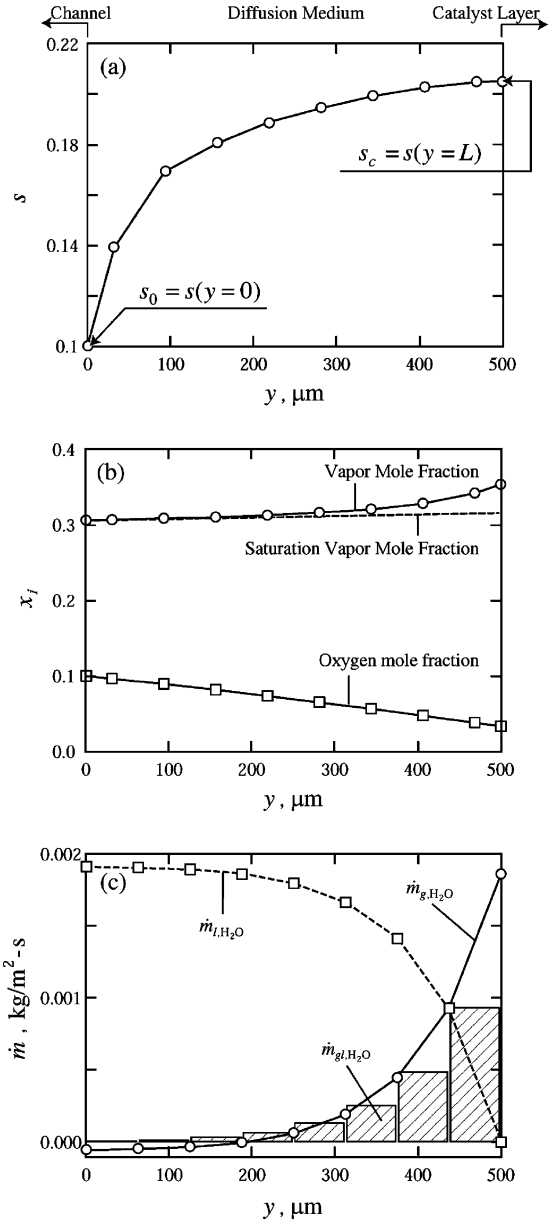

Fig. 9. Spatial distribution of: (a) water saturation, (b) concentrations and (c) condensation flux, vapor flux, and water flux, for current density $j_e = 1$ A/cm^2.

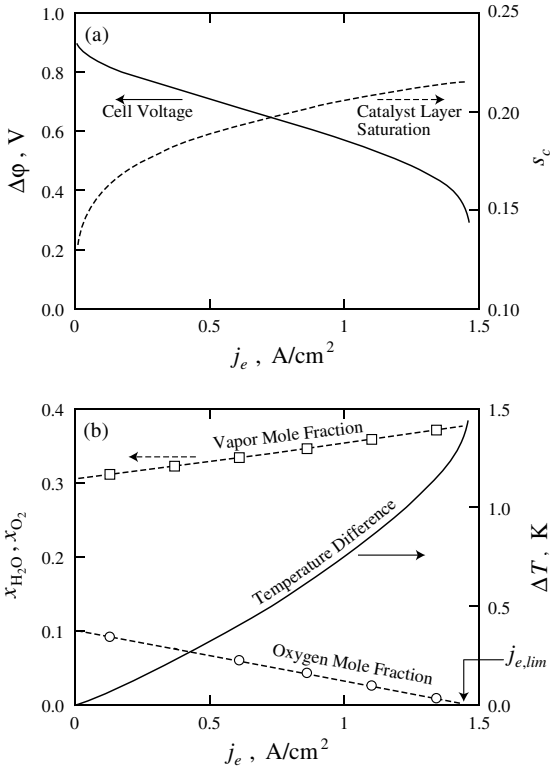

Fig. 10. Variation of: (a) cell voltage and catalyst layer saturation and (b) temperature difference across the diffusion medium and species concentrations at catalyst layer, with respect to current density.

medium. In case of $A_{lg}/V = 10,000$ m^2/m^3, the condensation occurs over about 100 m portion of the diffusion medium, and this indicates that full condensation of water vapor produced by reaction at $j_e = 1$ A/cm^2 requires about 1 m^2/m^2 of area specific interfacial area A_{lg}/A (same as nominal area). Since the solid/fluid specific interfacial area A_{sf}/V of a typical diffusion medium, determined from $4(1-\varepsilon)/d_f$, is about 3×10^5 m^2/m^3, A_{lg}/V of 10,000 m^2/m^3 is only about 3% of A_{sf}/V.

Fig. 12(a) shows the effect of variation in the specific interfacial area on the saturation at the catalyst layer s_c, and on the limiting current density $j_{e,lim}$. The results show that the higher condensation rates result in a higher water saturation in the diffusion medium, but this water saturation is not very sensitive to the condensation rate. Also the results show that regardless of the increase in the water saturation, the cell performance is enhanced (larger limiting current density) with the higher condensation rates. This is primarily due to the reduction in the vapor flux which acts as a convective resistance to the oxygen diffusion, and also due to the reduction in the vapor mole fraction in the catalyst layer. Thus to improve the fuel cell performance, we should optimize the capillary flow characteristics of the diffusion medium, while increasing the condensation rates as high as possible.

Fig. 12(b) shows the effect of change in the magnitude of the capillary pressure, characterized by $|dp_c/dS|$, i.e., increasing $|dp_c/dS|$ lowers the water saturation in the diffusion medium. The limiting current density also increases with $|dp_c/dS|$, primarily due to the lower diffusion resistance caused by the lower water saturation. Altering $|dp_c/dS|$ would require change in other

Table 1
Parameters and properties for simulation of water transport in diffusion medium

Porosity	ε	0.5
Diffusion medium thickness	L	0.5 mm
Fiber diameter	d_f	7 μm
Operation temperature	T	70 °C
Operation pressure	P	1 atm
Operation current density	j_e	1 A/cm^2
Oxygen mole fraction	$x_{O_2,\infty}$	0.1
Vapor mole fraction	$x_{H_2O,\infty}$	saturated
Hydrogen mole fraction	$x_{H_2,\infty}$	0.2
Immobile saturation	s_{im}	0.1
Surface reduced saturation	S_0	0.0
Specific interfacial area	A_{lg}/V	1000 m^2/m^3
Slope of capillary pressure	$\lvert dp_c/dS\rvert$	30,321 Pa
Absolute permeability	K	2.55×10^{-13} m^2
Surface tension	σ	0.0644 N/m
Cosine of contact angle	$\lvert\cos\theta_{c,a}\rvert$	0.5
Effective electro-osmotic drag	α_{eo}	0.5
Maximum reversible voltage	$\Delta\varphi^o$	1.253 V
Exchange current density	$j_{e,0}$	1 mA/cm^2
Total area specific resistance	r_t	0.15 Ω cm^2
Slope of Tafel plot	k_a	0.02 V
Concentration loss constant	k_c	0.05 V
Oxygen diffusivity	D_{m,O_2}	30.3 mm^2/s
Vapor diffusivity	D_{m,H_2O}	34.5 mm^2/s
Hydrogen diffusivity	D_{m,H_2}	114 mm^2/s
Heat of vaporization	Δh_{lg}	2,334,000 J/kg
Heat partition factor	a_l	2/3
Thermal conductivity	$\langle k\rangle$	4 W/m K
Density of water	25 ρ_l	978 kg/m^3
Viscosity of water	μ_l	0.000405 kg/m s

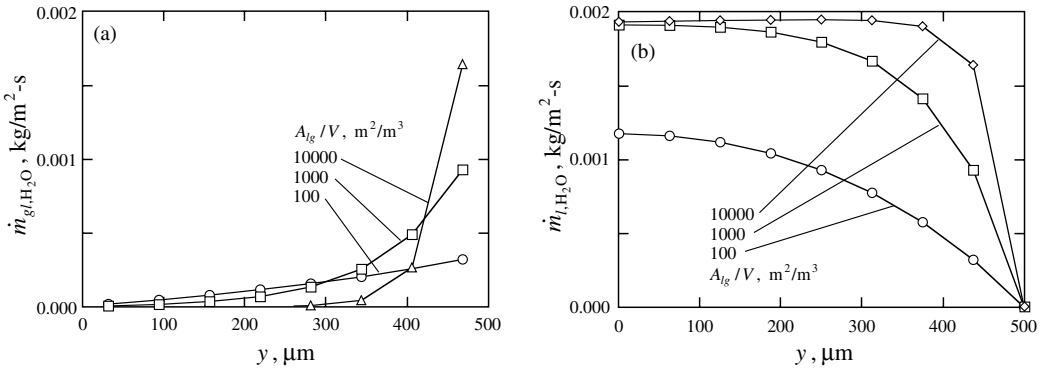

Fig. 11. Effect of liquid/gas specific interfacial area A_{lg}/V on spatial variation of: (a) condensation rate and (b) liquid water flux, for $j_e = 1$ A/cm^2 and $A_{lg}/V = 10^2$, 10^3, 10^4m^2/m^3.

geometric parameters, other than the hydrophobicity determined from the contact angle $\theta_{c,a}$. This apparent contact angle is determined from the PTFE content and its distribution in the diffusion medium. Then the hydrophobicity is also related to porosity ε (not a free parameter) as the PTFE coating can only be included with a sacrifice in the pore volume.

To increase $|dp_c/dS|$, we can reduce the fiber diameter. Fig. 12(c) shows this increase in the capillary pressure by reducing the fiber diameter, is not desirable, since a diffusion medium with larger fibers is preferred for reducing the water saturation. The small fiber size does increase $|dp_c/dS|(\propto 1/d_f)$, but it reduces the absolute permeability $K(\propto d_f^2)$. Thus the liquid water flux,

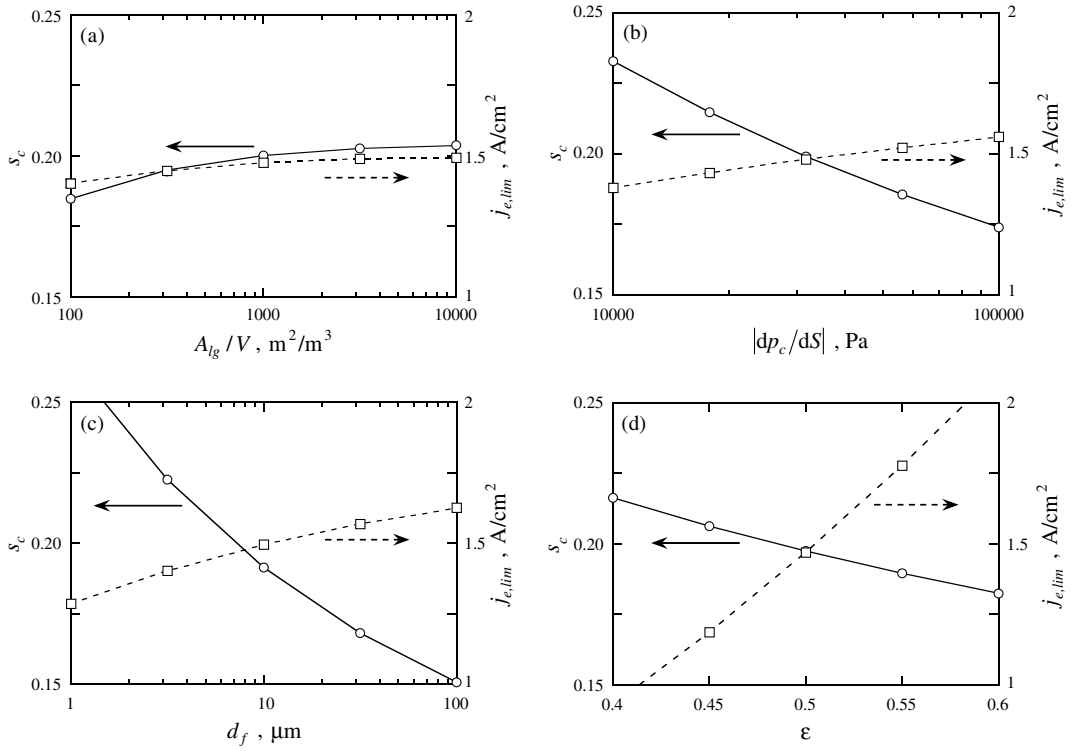

Fig. 12. Effect of variation in: (a) liquid/gas specific interfacial area A_{lg}/V, (b) gradient of capillary pressure $|dp_c/dS|$, (c) fiber size d_f and (d) porosity ε, on the catalyst layer saturation s_c at a current density of 1 A/cm^2 and the limiting current density $j_{e,lim}$. For the variation of the catalyst layer saturation with respect to porosity, a current density of 0.9 A/cm^2 is used.

which is proportional to the product of $|dp_c/dS|$ and K, decreases with decreasing fiber diameter.

To increase $|dp_c/dS|$, we can also decrease the porosity as shown in Fig. 12(d). However, the results show that the larger porosity is better for the reduction of water saturation, in spite of the increase in $|dp_c/dS|$. The effect of porosity on the limiting current density is more noticeable, and this also favors a larger porosity. From Fig. 12(d), we can infer the effect of hydrophobicity (PTFE content) on the cell performance. Due to the high sensitivity of the limiting current density on the porosity, increasing the hydrophobicity by adding more PTFE coating material is questionable.

Based on the parametric studies for a single-layer diffusion medium, we now proceed to the introduction of a two-layer diffusion medium, which partly removes these contradictory tendencies.

4. Enhancement of water transport using two-layer diffusion medium

Efforts continue to improve the water transport in the diffusion medium and to reduce the flooding of catalyst layer, and as was noted, the larger capillary pressure, porosity, and fiber diameter are advantageous (but are not compatible).

Consider expressing the capillary water flux, Eq. (16), as

$$\dot{m}_{l,H_2O} = -\frac{\rho_l K K_{rl}}{\mu_l}\left[\left(\frac{\partial p_c}{\partial S}\right)\nabla S + \left(\frac{\partial p_c}{\partial d_f}\right)\nabla d_f + \left(\frac{\partial p_c}{\partial \theta_{c,a}}\right)\nabla \theta_{c,a} + \left(\frac{\partial p_c}{\partial T}\right)\nabla T + \cdots\right]. \quad (42)$$

This suggests the role of the spatial gradient of several parameters, in enhancing the water transport. Now, by introducing the spatial variation of the fiber size, hydrophobicity, etc., the water transport can be maximized by utilizing the additional driving forces for the water transport. The above equation also suggests that maintaining isothermal condition is desirable.

By introducing macropores (around 50–100 μm in pore size) into the diffusion medium, Kong et al. [27] obtained a better cell performance. The macropores readily accumulate water in neighboring pores and form flow paths which are less resistive. So the macropores wick in more water, while reducing the water saturation in the micropores. Thus the liquid and gas phase are effectively separated.

Experiments have demonstrated the advantage of placing a thin microlayer (made of fine carbon particles and PTFE) between the diffusion medium and the catalyst layer [28,29]. The role of the microlayer is explained with the concept of the capillary barrier, commonly used to protect a specific region from contamination in underground water transport. Regions with coarse-grained particles prevent the liquid water accumulation, as capillary pressure there is less than the rest (hydrophilic).

Fig. 13(a) shows the capillary pressure curves for two hydrophobic porous media. Porous medium I has a smaller characteristic capillary radius r_c, compared to medium II, which is achieved by changing the fiber diameter d_f or the porosity ε. When partially saturated (e.g., $S = 0.2$) porous media I and II are brought together, the saturation distribution in each porous medium evolves to make the capillary pressure p_c uniform everywhere. This requires the transport of water from the medium I to II (fine to coarse medium) and the resulting saturation jump is shown in Fig. 13(b).

When using a microlayer (smaller r_c) near the catalyst layer, the water condensed in the diffusion medium cannot readily penetrate into the catalyst layer. This additionally reduces the water saturation in the catalyst layer, as water saturation environment in the diffusion medium is effectively screened by the microlayer.

The concept of the saturation jump is useful for enhancement of the water transport capability of the diffusion medium. The hydrophobic, two-layer, diffusion media made of fine and coarse fiber layers are shown in Fig. 14. We assume that water condenses in a thin condensation zone in the inner region near the catalyst layer and flows with constant flux from right to left. Due to the distributed condensation, the water flux is largest at the diffusion medium/channel interface, but for large A_{lg}/V, the water flux $\dot{m}_{l,H_2O}$ becomes rather uniform throughout the diffusion medium, as shown in Fig. 11(b). Then the water saturation distribution is obtained

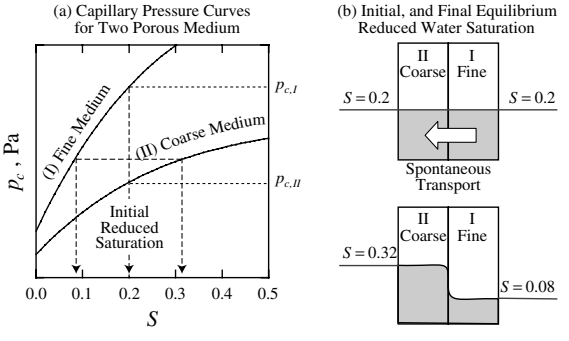

Fig. 13. Jump in saturation across the interface of porous media I and II, due to discontinuity of capillary characteristics. Medium I has finer pore structure compared to medium II.

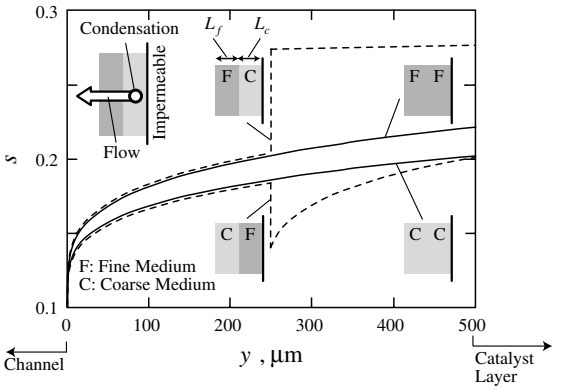

Fig. 14. Saturation distributions in two-layer diffusion medium, with constant flux of liquid water flowing from right to left. Four double layers are shown, fine–fine, fine–coarse, coarse–coarse and coarse–fine. The difference between the fine and coarse layers is the fiber diameter, $d_{f,f} = 1/2d_{f,c}$, and $L_f = L_c$.

as shown in Fig. 14, using the saturation jump condition (from the continuity of capillary pressure) at the interface of fine/coarse fibrous layers.

Fig. 14 shows that the order of placement of the fine- and coarse-fiber layers matters greatly. The results are for $L_f = L_c$, and $d_{f,f} = 1/2d_{f,c}$. Placing the fine-fiber layer between the coarse one and the catalyst layer (similar to microlayer) is optimal for reduction of the water saturation in the diffusion medium. The coarse-fiber layer transports liquid water with less flow resistance (larger permeability), while the fine-fiber one reduces water saturation with a higher capillary pressure.

The thickness of the coarse layer L_c is varied (while the total thickness is maintained constant) to investigate its effect on the water saturation and the cell performance. The fiber diameter of the coarse layer is twice that of the fine layer, the same as above (Table 2 gives the other parameters). The uniform liquid water flux can be related to the current density as

$$\dot{m}_{l,H_2O} = M_{H_2O}\frac{j_e}{2F}(1+2\alpha_{eo}) = -\rho_l\frac{KS^3}{\mu_l}\left|\frac{dp_c}{dS}\right|\frac{dS}{dy}. \quad (43)$$

Integration of the above equation for the coarse layer results in the saturation distribution

Table 2
Capillary flow parameters for simulation of the two-layer diffusion medium

Properties	Coarse layer	Fine layer
d_f	2 μm	1 μm
K	1×10^{-12} m^2	0.25×10^{-12} m^2
$\lvert dp_c/dS\rvert$	10,000 Pa	20,000 Pa
p_0	0 Pa	0 Pa

$$S(y) = (4a_c y + S_0^4)^{1/4} \quad (0 < y < L_c), \tag{44}$$

where a_c is

$$a_c = \frac{\dot{m}_{l,H_2O}\mu_l}{\rho_l K_c |dp_c/dS|_c}, \tag{45}$$

and S_0 is the surface reduce saturation (assumed zero here).

At the interface of the two layers ($y = L_c$), there is a jump in the reduced saturation from S_{i-} (in the coarse layer) to $S_{i,+}$ (in the fine layer). S_{i-} is determined from Eq. (44) as

$$S_{i,-} = S(L_c) = (4a_c L_c + S_0^4)^{1/4}. \tag{46}$$

Assuming that the immobile saturation s_{im} of the two layers is same, the capillary pressures are linear functions of the reduced saturation given by

$$\begin{aligned} p_{c,c} &= p_{0,c} + \left|\frac{dp_c}{dS}\right|_c S, \\ p_{c,f} &= p_{0,f} + \left|\frac{dp_c}{dS}\right|_f S, \end{aligned} \tag{47}$$

and that the capillary pressures at zero reduced saturation, $p_{0,c}$ and $p_{0,f}$, are negligible, then the continuity of capillary pressure gives the saturation jump condition as

$$S_{i,+} = \frac{|dp_c/dS|_c}{|dp_c/dS|_f} S_{i,-} = \frac{1}{2} S_{i,-} \quad (y = L_c). \tag{48}$$

The saturation distribution in the fine-fiber layer is found similar to Eq. (44), as

$$S(y) = (4a_f(y - L_c) + S_{i,+}^4)^{1/4} \quad (L_c < y < L), \tag{49}$$

and the maximum reduced saturation at the diffusion medium/catalyst layer interface S_c is

$$\begin{aligned} S_c &= (4a_c(L - L_c) + S_{i,+}^4)^{1/4} \\ &= \left(\frac{1}{16}S_0^4 + 8a_c L - \frac{31}{4}a_c L_c\right)^{1/4}, \end{aligned} \tag{50}$$

where $a_f = 2a_c$.

The predicted water saturation distribution in the two-layer diffusion medium is shown in Fig. 15(a), for three different partitions, which shows that two-layer diffusion medium can increase the water saturation. The fine-fiber layer should be thin to reduce the water saturation within the diffusion medium and near the catalyst layer. The saturation jumps and the saturation at the catalyst layer, given as functions of thickness of the coarse-fiber layer, shown in Fig. 15(b), suggests that the fine-fiber layer should be less than 1/3 of total thickness to be effective.

Using Eq. (13) to obtain the effective diffusivity, Fig. 15(c) shows that the effective diffusivity with the diffusion medium averaged saturation $\langle s \rangle$ is optimal when it is made with $L_c/L = 0.7$. Though the transport of water from the fine- to the coarse-fiber layer reduces the water saturation in the diffusion medium, the gain in the

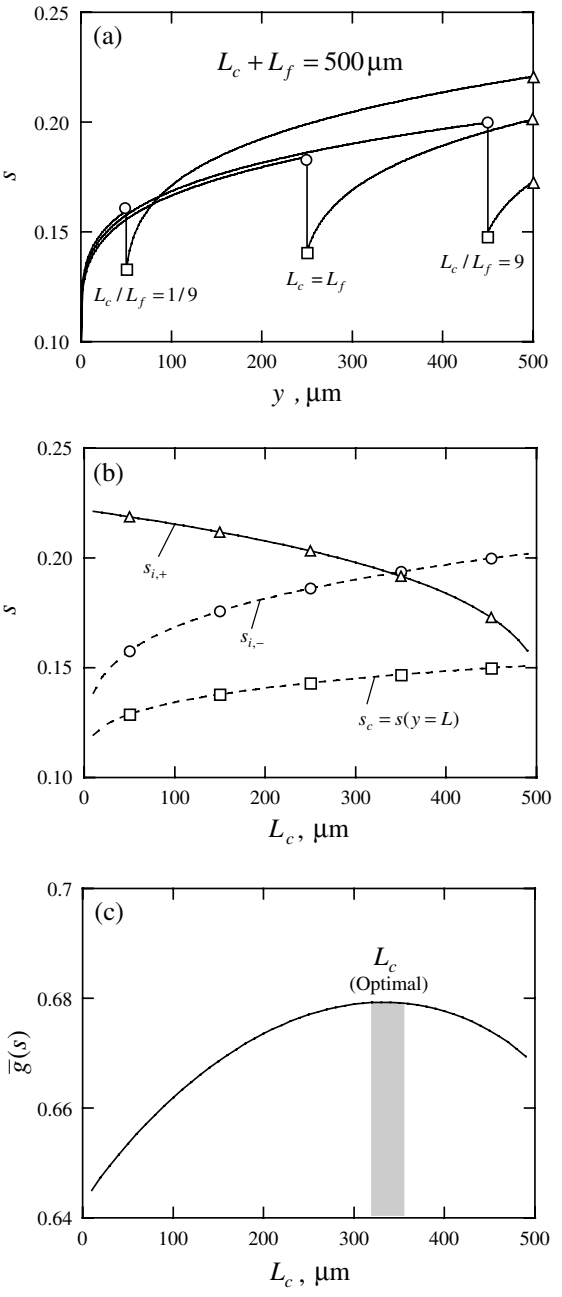

Fig. 15. Effect of partition of the diffusion medium into fine and coarse layers, with constant total length $L_c + L_f = 500$ μm. (a) Water saturation distribution for three different partitions, (b) the variations of water saturation jumps $s_{i,-}$ and $s_{i,+}$, and the saturation at the catalyst layer $s_c = s(y = L)$, with respect to the coarse layer thickness and (c) variation of the averaged saturation factor $\bar{g}(s)$ and its maximum value for enhanced diffusion.

effective diffusivity (due to saturation reduction of two-layer structure) is not large.

5. Summary

The porosity and saturation dependence of the effective diffusivity of fibrous diffusion media have been determined using the network models for anisotropic solid structure and liquid water distribution. The results are given by Eq. (13).

The water saturation distribution is predicted using a one-dimensional description of the water vapor condensation kinetics, species mass diffusion, and capillary motion of the condensate in a hydrophobic fibrous diffusion medium. The effects of the fiber diameter, porosity, and capillary pressure on the water saturation and the cell performance are examined and it is shown that in a single-layer diffusion media there are contradictory tendencies.

Then the two-layer diffusion medium is introduced for an optimal cell performance. It is shown that by creating a saturation jump across a fine and a coarse layer and by placing the fine layer adjacent to the catalyst layer (similar to the conventional microlayer), the cell performance is improved. The design specifics of the optimized two-layer diffusion medium are suggested.

Acknowledgements

The financial and technical support of Plug Power Incorporated is greatly appreciated. J.H. Nam also thanks the Korean BK21 program for the partial financial support.

References

[1] J. Larminie, A. Dicks, Fuel Cell Systems Explained, Wiley, New York, 2000.
[2] D.M. Bernardi, M.W. Verbrugge, Mathematical model of a gas diffusion electrode bonded to a polymer electrolyte, AIChE J. 137 (1991) 1151–1163.
[3] G.J.M. Janssen, A phenomenological model of water transport in a proton exchange membrane fuel cell, J. Electrochem. Soc. 148 (2001) A1313–A1323.
[4] V. Gurau, H. Liu, S. Kakac, A two dimensional non-isothermal mathematical model for proton exchange membrane fuel cells, AIChE J. 44 (1998) 2410–2422.
[5] J.S. Yi, T.V. Nguyen, Multicomponent transport in porous electrodes of proton exchange membrane fuel cells using the interdigitated gas distributors, J. Electrochem. Soc. 146 (1999) 38–45.
[6] W.H. He, J.S. Yi, T.V. Nguyen, Two-phase flow of the cathode of pem fuel cells using interdigitated flow fields, AIChE J. 46 (2000) 2053–2064.
[7] D. Natarajan, T.V. Nguyen, A two-dimensional, two-phase, multicomponent, transient model for the cathode of a proton exchange membrane fuel cell using conventional gas distributor, J. Electrochem. Soc. 148 (2001) A1324–A1335.
[8] Z.H. Wang, C.Y. Wang, K.S. Chen, Two-phase flow and transport in the air cathode of proton exchange membrane fuel cells, J. Power Sources 94 (2001) 40–50.
[9] M.M. Mezedur, M. Kaviany, W. Moore, Effect of pore structure, randomness and size on effective mass diffusivity, AIChE J. 48 (2002) 15–24.
[10] M.M. Tomadakis, S.V. Sotirchos, Ordinary and transition regime diffusion in random fiber structures, AIChE J. 39 (1993) 397–412.
[11] S. Li, J. Lee, J. Castro, Effective mass diffusivity in composite, J. Compos. Mater. 36 (2002) 1709–1724.
[12] J. Whitcomb, X. Tang, Micromechanics of moisture diffusion in composite with impermeable fibers, J. Compos. Mater. 36 (2002) 1093–1101.
[13] R.B. Bird, W.E. Stewart, E.N. Lightfoot, Transport Phenomena, Wiley, New York, 1960.
[14] J. Schwarzbach, Diffusion in porous materials partially wetted with a binary mixture, Chem. Eng. Process. 26 (1989) 35–44.
[15] M. Aubertin, M. Aachib, K. Authier, Evaluation of diffusive gas flux through covers with GCL, Geotext. Geomembranes 18 (2000) 215–233.
[16] N.S. Martys, Diffusion in partially-saturated porous materials, Mater. Struct. 32 (1999) 555–562.
[17] K. Hanamura, M. Kaviany, Propagation of condensation front in steam injection into dry porous media, Int. J Heat Mass Transfer 38 (1995) 1377–1386.
[18] M. Kaviany, Principles of Heat Transfer in Porous Media, second ed., Springer, New York, 1999.
[19] J. Bico, C. Marzolin, D. Quéré, Pearl drops, Europhys. Lett. 47 (1999) 220–226.
[20] S.E. Schwartz, Historical perspective on heterogeneous gas-particle interaction, Mass Accommodation Workshop, Aerodyne Research Incorporated, Billerica, MA, 2002.
[21] H. Kim, P.S.C. Rao, M.D. Annable, Determination of effective air–water interfacial area in partially saturated porous media using surfactant adsorption, Water Resour. Res. 33 (1997) 2705–2711.
[22] R.G. Larson, L.E. Scriven, H.T. Davis, Percolation theory of two phase flow in porous media, Chem. Eng. Sci. 36 (1981) 57–73.
[23] C. Du, Y.C. Yortsos, A numerical study of the critical gas saturation, Transport Porous Med. 35 (1991) 205–225.
[24] N.R. Morrow, Irreducible wetting-phase saturation in porous media, Chem. Eng. Sci. 25 (1970) 1799–1815.
[25] M. Kaviany, Principles of Heat Transfer, Wiley, New York, 2001.
[26] S. Shimpalee, S. Dutta, Numerical prediction of temperature distribution in pem fuel cells, Numer. Heat Transfer A 38 (2000) 111–128.
[27] C.S. Kong, D.-Y. Kim, H.-K. Lee, Y.-G. Shul, T.-H. Lee, Influence of pore-size distribution of diffusion layer on mass-transport problems of proton exchange membrane fuel cells, J. Power Sources 108 (2002) 185–191.
[28] B. Muller, T. Zawodzinski, J. Bauman, E. De Castro, M. De Marinis, Carbon cloth gas diffusion backing for high performance PEFC catodes, in: S. Gottesfeld, T.F. Fuller,

G. Halpert (Eds.), Proceedings of Proton Exchange Membrane Fuel Cells, Second International Symposium, Electrochemical Society, Boston, MA, 1998, pp. 1–9.

[29] Z. Qi, A. Kaufman, Improvement of water management by a microporous sublayer for PEM fuel cells, J. Power Sources 109 (2002) 38–46.